

1 **Tsunami Inundation Modeling in Constructed Environments: A Physical and**  
2 **Numerical Comparison of Free-Surface Elevation, Velocity, and Momentum Flux.**

3 Hyongsu Park\*

4 Graduate Research Assistant, School of Civil and Construction Engineering, Oregon State  
5 University, Corvallis, OR 97331-2302, USA, Email: Hyongsu.park@gmail.com, Tel: 1-  
6 541-602-8618, Fax: 541-737-3052

7 Daniel T. Cox

8 Professor, School of Civil and Construction Engineering, Oregon State University, Corvallis,  
9 OR 97331-2302, USA, Email: dan.cox@oregonstate.edu

10 Patrick J. Lynett

11 Associate Professor, Dept. of Civil and Environmental Engineering, University of Southern  
12 California, Los Angeles, CA 90089-2531, USA, Email: plynett@usc.edu

13 Dane M. Wiebe

14 Graduate Research Assistant, School of Civil and Construction Engineering, Oregon State  
15 University, Corvallis, OR 97331-2302, USA, Email: wiebed@onid.orst.edu

16

17 Sungwon Shin

18 Assistant Professor, Department of Energy Plant, College of Engineering, Kwandong  
19 University, 522 Naegok-dong, Gangneung, Gangwon-do, 210-701, Korea,  
20 Email: sungwshin@gmail.com

21 \* Corresponding Author

22 **Abstract**

23 A laboratory benchmark test for tsunami inundation through an urban waterfront  
24 including free surface elevation, velocity, and specific momentum flux is presented and  
25 compared with a numerical model (COULWAVE). The physical model was a 1:50 scale  
26 idealization of the town Seaside, Oregon, designed to observe the complex tsunami flow  
27 around the macro-roughness such as buildings idealized as impermeable, rectangular blocks.  
28 Free surface elevation and velocity time series were measured and analyzed at 31 points  
29 along 4 transects. Optical measurements of the leading bore front were used in conjunction  
30 with the in-situ velocity and free surface measurements to estimate the time-dependent  
31 specific momentum flux at each location. The maximum free surface elevation and specific  
32 momentum flux sharply decreased from the shoreline to the landward measurement locations,  
33 while the cross-shore velocity slowly decreased linearly. The experimental results show that

34 the maximum specific momentum flux is overestimated by 60 to 260%, if it is calculated  
35 using the each maximum values of the free surface elevation and cross-shore velocity.  
36 Comparisons show that the numerical model is in good agreement with the physical model at  
37 most locations when tuned to a friction factor of 0.005. When the friction factor decreased by  
38 a factor of 10 (from 0.01 to 0.001), the average maximum free surface elevation increased  
39 15%, and the average cross-shore velocity and specific momentum flux increased 95 and  
40 208%, respectively. This highlights the importance of comparing velocity in the validation  
41 and verification process of numerical models of tsunami inundation.

42 **Keywords:** Tsunami, Inundation, Macro-roughness, Benchmark, COULWAVE,  
43 Friction factor.

44

45 **1.1 Introduction**

46           Tsunamis are unpredictable natural events which are most commonly associated with  
47 large magnitude earthquakes along coastal plate boundaries. For near field events, the first  
48 waves often arrive in the tens of minutes, leaving little time for preparation or evacuation,  
49 and can inundate several kilometers inland. Tsunamis, such as the 2004 Indian Ocean event,  
50 delivered widespread damage to coastal communities both near and far from the epicenter,  
51 and caused casualties in the hundreds of thousands, which is devastating both locally and  
52 regionally (Imamura *et al.*, 2006). The most recent tsunami occurred on March 11th, 2011 in  
53 the north-western Pacific Ocean 72 km east of the Oshika Peninsula of Tōhoku, Japan. This  
54 event resulted in 15,844 fatalities 3,394 missing peoples and damaged 128,530 houses,  
55 230,332 buildings and 78 bridges (Mori *et al.*, 2011).

56           To minimize casualties and damage from future events, a deeper understanding of  
57 tsunamis is required, particularly for the complex flows associated with the tsunami  
58 inundation and the return flow over complex bathymetry and around structures. Due to the  
59 increasing computational power and maturation of numerical schemes, the numerical  
60 modeling of tsunami inundation is becoming increasingly important for tsunami mitigation  
61 (e.g., Lynett, 2007). However, some simplifications of the numerical schemes are required,  
62 particularly with respect to the problem of turbulence closure, and to extend the model over a  
63 sufficiently large domain (e.g., several km to encompass a coastal community).

64           To model the tsunamis hazard for coastal communities accurately, the constructed  
65 environment must be incorporated into the numerical model as it strongly influences the  
66 hydrodynamics. The 2004 Indian Ocean Tsunami field survey highlighted the importance of  
67 coastal structures in mitigating tsunami damage (Dalrymple and Kriebel, 2005; Tomita *et al.*,  
68 2006). After the 2011 Great East Japan Tsunami, the field survey also highlighted that

69 tsunami damage is strongly dependent on location and environment (Yeh *et al.*, 2012). Yeh  
70 (2006) showed that the hydrodynamic force of the tsunami on structures in the inundation  
71 zone is proportional to the momentum flux, which is the inundation depth multiplied by the  
72 squared velocity and it can be related to the probability of damage (*e.g.*, Koshimura *et al.*  
73 2009a; Koshimura *et al.* 2009b; FEMA, 2008).

74 It is also necessary to benchmark these models performance in terms of predicting  
75 the free surface and velocity as well as their sensitivity to tuning parameters. Several  
76 benchmark tests are prevailing as standard verification methods for the numerical modeling  
77 of tsunamis (Yeh *et al.*, 1996; Synolakis *et al.*, 2007; Liu *et al.*, 2008) such as exact solutions  
78 and physical model data of solitary waves on simple sloped beaches (Synolakis, 1987) and on  
79 compound sloped beaches (Kânoğlu and Synolakis, 1998), large scale conical island physical  
80 model (Briggs *et al.*, 1995), and runup on a complex three-dimensional coast (Hokkaido  
81 Tsunami Survey Group, 1993). In addition, landslide tsunamis generated by submarine mass  
82 failure received much attention after the 1998 Papua New Guinea tsunami, and a three  
83 dimensional landslides experiment (Synolakis, 2003) was performed as a benchmark test.  
84 Even though most casualties and damage from tsunamis are related to the complex  
85 inundation flow, which includes wave breaking near the shoreline and interaction with  
86 coastal structures, the most advanced numerical models and benchmark tests only provide the  
87 maximum run-up heights or a time series of free surface elevation. Complex flows are  
88 difficult to both estimate due to the required computing power and validate due to the  
89 absence of proper benchmark tests. As a result, most numerical models focused on the  
90 estimation of tsunami propagation, and calculation of arrival times and maximum runup  
91 heights.

92 Several studies related to macro-roughness and tsunami velocity variation have been  
93 performed. Cox *et al.* (2008) performed physical model tests of Seaside, Oregon, which

94 showed that the macro-roughness reduced the tsunami inundation velocity by 40% (Rueben  
95 *et al.*, 2010). The reduction in runup elevations and maximum overland velocities due to  
96 obstructions have been studied numerically (Lynett, 2007) and Tomita and Honda (2007)  
97 highlighted that the resulting inundation area and depth from the numerical model with  
98 macro-roughness was in good agreement with the actual inundation observed in Galle city,  
99 Sri Lanka from the 2004 Indian Ocean Tsunami. Other studies on the influence of macro-  
100 roughness element arrays compared the free surface elevation of numerical and physical  
101 model results (Goseberg and Schlurmann, 2010), and the effect of bed slope and bottom  
102 friction on maximum tsunami runup height and velocity using numerical models (Apostos *et*  
103 *al.*, 2011). More recently, the importance of artificial and natural structures on tsunami  
104 mitigation was studied through a numerical and field study (Nandasena *et al.*, 2012).

105 In this project, we present a model study of tsunami flow over and around macro-  
106 roughness in the idealized physical model of Seaside, Oregon, and provide a new data set of  
107 free surface elevation, velocity, and momentum to be used as a benchmark test. This data set  
108 was used to validate the numerical model results from COULWAVE (Lynett *et al.*, 2002).  
109 This paper is outlined as follows. Section 2 presents the large-scale physical model basin,  
110 measurement devices and their locations, describes the model data analysis, and shows the  
111 results of the experiment. Section 3 presents the numerical model setup. Section 4 presents a  
112 comparison between the physical and numerical model. Section 5 concludes the paper with  
113 summary findings and ideas for future work.

## 114 **2.1 Model Design Setup**

115 The physical model was an idealized representation of Seaside, Oregon, located in  
116 the Pacific Northwest, United States constructed at 1:50 undistorted scale. There are several  
117 reasons why this site was chosen for study. One, The Cascadia Subduction Zone (CSZ) has a  
118 high potential hazard for the tsunami event in near future. Over the past 10,000 years the CSZ

119 has shown three typical ruptures scenarios: a rupture of 200 – 450 km of the southern margin  
120 with 18-20 events on the order of 8.2 Mw, a rupture of 650 km starting at the southern margin  
121 with 3-4 events on the order of 8.5 Mw, and a full length rupture with 19-20 events on the  
122 order of 8.9 Mw (Goldfinger, et al., 2012). The average recurrence interval between CSZ  
123 events is 240 years, and the next event is estimated to have a 7-12% probability of occurrence  
124 in the next 50 years (Goldfinger, et al., 2012). Two, the simple bathymetry of shore parallel  
125 contours and a large onshore spit. And three, the high concentration of residential and  
126 commercial buildings concentrated near the water front and located well within the expected  
127 tsunami inundation zone. Fig. 1 shows the expected extent of inundation from the CSZ event  
128 tsunami (solid line) (DOGAMI, 2001), the dimensions of the physical model basin (dash-dot  
129 line), and the dimensions of the physical model with macro-roughness (dashed line). The  
130 inset map within Fig. 1 shows the location of Seaside, Oregon, on a region scale, the  
131 proximity to the CSZ, and the location of the Deep-ocean Assessment and Reporting of  
132 Tsunamis (DART) buoys (NOAA, 2012).

133 Plan and elevation views of the physical model in the Tsunami Wave Basin at O.H.  
134 Hinsdale Wave Research Laboratory, Oregon State University, are shown in Fig. 2. The  
135 background images are satellite imagery of Seaside and a photo of the top view of the  
136 physical model (Rueben *et al.*, 2010). The origin of the  $x$  and  $y$  axes was centered on the  
137 wavemaker, with the  $x$  positive onshore and the  $y$  positive to the north. The rectangular basin  
138 was 48.8 m long, 26.5 m wide, and 2.1 m deep, and was equipped with a segmented, piston-  
139 type wavemaker with a maximum stroke of 2.1 m and maximum velocity of 2.0 m/s (Cox *et*  
140 *al.*, 2008). The idealized bathymetry for Seaside was constructed of smooth concrete with a  
141 flat finish, and an estimated roughness height of 0.1-0.3 mm (Rueben *et al.*, 2010). The  
142 profile consisted of a 10 m horizontal section near the wavemaker with a depth of 0.97 m, an  
143 8 m section at a 1:15 slope, a 15 m section at a 1:30 slope, on which the SWL intersected, and

144 another horizontal section 11 m in length which extended to the back wall. The idealized  
145 buildings which created the macro-roughness elements were fixed in place on the upper  
146 horizontal section to provide repeatability between tests. Four surface piercing wire resistance  
147 wave gages (WG1-WG4) were fixed in the basin at the following locations: WG1 (2.086 m, -  
148 0.515 m), WG2 (2.068 m, 4.065 m), WG3 (18.618 m, 0.000 m), and WG4 (18.618, 2.860 m).

149 A detailed plan view of the macro-roughness elements is shown in Fig. 3 in the same  
150 orientation as Fig. 1 and Fig. 2, with the Pacific Ocean to the left. In the model, the town is  
151 fronted by a 2 m (prototype scale) seawall. The blocks represent large hotels or commercial  
152 buildings, light commercial buildings, and residential houses, and the thick solid black lines  
153 between the blocks represent city streets. The buildings were positioned on the flat ground  
154 using aerial imagery and field survey data. The Necanicum River which flows through the  
155 center of Seaside ( $x = 42$  m), was not included in the model, and is only referenced with blue  
156 paint. Other parameters not taken into account by the physical model include vegetation,  
157 debris, sediment, and other small-scale roughness effects. The white boxes labeled A to D  
158 and 1 through 9, represent measurement locations of free surface elevation and velocity.  
159 Measurement locations are divided into 4 lines; A to D. Line A is located on a city street  
160 parallel to the primary inundation flow direction and numbered sequential 1 to 9, as the  
161 measurement locations move inland. Lines B and C are on streets inclined approximately  $10^\circ$   
162 to the flow direction, are flanked by hotels or commercial buildings, and numbered the same  
163 as Line A. Line D is located mostly behind buildings and only had 4 measurement locations.  
164 In total there were 31 measurement locations.

165 Four pairs of co-located ultra-sonic surface wave gages (USWG, Senix Corporation  
166 TS-30S1-IV) and acoustic-Doppler velocimeters (ADV, Nortec Vectrino) sensors were used  
167 to measure the free surface and flow velocity in Lines A, B, C, and D, simultaneously.  
168 Through the experiment, the sensors in lines A, B, and C moved in unison from Positions 1

169 through 9 and have the same number of repetitions for lines A, B, and C at a given location as  
170 indicated in Table 1. The sensors in Line D moved somewhat independently as listed in  
171 Table 1 with the aim of extracting turbulence statistics although this proved to be problematic  
172 due to the initial air entrainment. For the single tsunami wave condition, the total number of  
173 trials,  $N_T$ , was 136, of which the total number of acceptable trials,  $N_V$ , which were suitable  
174 for analysis was 99. The majority of trials ( $N_T = 53$ ) were performed with all the sensors  
175 located at Position 1 to collect statistics of turbulence due to the wave breaking. Because of  
176 time constraints, the number of trials performed at the remaining locations decreased;  
177 however, an adequate number of trials were still performed to provide reliable ensemble  
178 averages. Table 1 lists the coordinates of each measurement location and the total number of  
179 trials performed and available. Again, the origin of the coordinates is the center of the wave  
180 maker (Fig. 2).

181 The design tsunami condition produced by the wavemaker used an error function to  
182 maximize the full 2.0 m stroke, and had a duration of 10.0 s. The wave height measured at  
183 WG1, over the horizontal section of the basin, was approximately 0.20 m. At prototype scale,  
184 this wave height is 10 m, which corresponds to the estimated tsunami wave height for the  
185 “500-yr” CSZ tsunami for this region (Tsunami Pilot Study Working Group, 2006).

## 186 **2.2 Model Results**

187 This section presents the measured time dependent and cross-shore variability of  
188 maximum free surface displacement, velocity, and momentum flux. Fig. 4a shows the wave-  
189 maker paddle displacement,  $S$  (solid line), as a function of time and the free surface elevation  
190 on the paddle (dashed line) for Trial 51. Fig. 4b shows the measured time series of free  
191 surface elevation at WG1 (solid line) and WG3 (dashed line) for Trial 51. WG 1 and 3 were  
192 located 2.0 m and 18.6 m from the wavemaker, and had peak elevations of 0.17 and 0.20 m,  
193 respectively. The shape of wave at WG3 was asymmetric and pitched forward as it passed the



194 change in bathymetry. At  $t = 35$  s, reflected waves were detected at WG3 due to wave  
195 interaction on the shoreline and front row of buildings. The variability between runs can be  
196 estimated by comparing the standard deviation of the signal to the full scale value. In Table 2,  
197  $\sigma_i$  is the standard deviation at the maximum of the ensemble averaged value and  $i$  is the time  
198 corresponding to the maximum ensemble averaged value.  $(X_i)_m$  is the full scale value at that  
199 time. For consistency, the statistics were computed using only the first 20 runs for each of  
200 the values listed in Table 2 although some quantities has a much larger number of realizations.  
201 Comparisons are made of the ratio of the standard deviation of the signal at the time of the  
202 maximum value to maximum ensemble averaged value,  $\sigma_i / (X_i)_m$  expressed as a percent. The  
203 variability is extremely low for the wavemaker displacement (0.14%), and low for the free  
204 surface elevation measured before breaking in the middle of the basin (less than 1.2%). After  
205 breaking, the variability increases to approximately 5% of the full scale value. The largest  
206 variation at D4 (8.2%) occurs behind the second row of buildings in the area where large  
207 eddies were observed. Fig. 4c and 4d show the time series of free surface elevation and  
208 cross-shore velocity for Trial 51 at A1 (solid line) and C1 (dash line). The maximum free  
209 surface elevation,  $(\eta)_m$ , and maximum cross-shore velocity,  $(u)_m$ , were 0.25 and 0.18 m and  
210 1.45 and 1.85 m/s at A1 and C1, respectively. The USWG and ADV sensors were intended to  
211 measure the instantaneous velocity over land; however, the ADV sensor only detected  
212 velocities after  $t = 26.4$  s, which was 1.3 s after the USWG sensor recorded the changes in the  
213 free surface elevation. The leading edge velocity was determined using optical measurements  
214 (Reuben et al., 2010) and an interpolation was used to replace the missing velocity data as  
215 explained in the next paragraph.

216 Fig. 5a shows the time series of ensemble averaged free surface elevation,  $\langle \eta \rangle$ ,  
217 ensemble averaged cross-shore velocity,  $\langle u \rangle$ , and ensemble averaged momentum flux per  
218 unit mass per unit width,  $\langle M \rangle$ , at A1. The momentum flux per unit mass per unit width,

219 hereafter called the specific momentum flux for brevity, is generally calculated as  $Hu^2$ , where  
 220  $H$  is the total water depth, calculated by subtraction of vertical datum,  $h$ , from free surface  
 221 elevation,  $\eta$ . Assuming Froude similitude would govern the scaling of the specific momentum  
 222 flux (Hughes, 1993), the momentum flux per unit mass per unit width shown in Figure 5 and  
 223 6 would be proportional to the length scale squared or would be multiplied by  $2.5 \times 10^3$  to  
 224 convert to prototype conditions. Fig. 5b shows the number of recorded data for free surface  
 225 elevation,  $N_\eta$ , and cross-shore velocity,  $N_u$ , at each time step for location A1. The total  
 226 number of available trials,  $N_V$ , at A1 was 48 (Table 1). For the USWG, there were some  
 227 dropouts in the free surface measurements before the arrival of the bore ( $t < 25.1$  s) and the  
 228 number of available measurements was approximately  $N_\eta = 40$ . After arrival of the bore, the  
 229 sensor accurately captured the free surface elevation and  $N_\eta = N_V = 48$ . For the ADV, due to  
 230 air entrainment in the leading edge of the bore, no data were collected for  $25.1 < t < 26.4$  s.  
 231 After 26.4 s, the number of trials for which data were available increased as shown in Fig 5b  
 232 (open circles) with  $N_u > 40$  at around  $t = 28.5$  s, leading to a stable estimate of the velocity as  
 233 can be seen in Fig 5a. To obtain an estimate of the missing data, the leading wave velocities  
 234 were analyzed by tracking the leading edge trajectory of each time step using two high  
 235 resolution video cameras mounted on the ceiling of the wave basin (Rueben *et al.*, 2010).

236 A second order polynomial curve (slender lines) was fit from the leading velocity  
 237 (filled circle) to the ensemble averaged ADV data at  $t = 28.5$  s. The velocity was assumed to  
 238 increase linearly from zero (recorded by the USGW) to the leading edge velocity. The  
 239 ensemble averaged specific momentum flux  $\langle M \rangle$  was estimated from the ensemble  
 240 estimates of the total water depth and the measured and interpolated velocity,

$$241 \quad \langle M \rangle = \langle H \rangle \cdot \langle u \rangle^2$$

242 The same procedure was performed at each measurement location, and the results at  
 243 A8 are shown in Fig. 6. For A8, the ADV was able to capture more of the leading wave

244 velocity because there was less air entrainment at A8. However, there was still some missing  
245 velocity data, and the same curve fitting procedure was used. The work of Rueben et al.  
246 (2010) successfully estimated the leading velocity for the same experimental setup using two  
247 overhead cameras with overlapping fields of view to capture the inundation along the length  
248 of the basin from  $25 < x < 43$  m and from  $-7 < y < 7$  m across the basin where the  $x$  and  $y$   
249 coordinates are defined in Figure 2 and includes the area shown in Figure 3. The two cameras  
250 were synchronized, and the images were rectified to the known elevation of the model at 1 m  
251 above the basin floor. The arrival time of the bore at locations in the image corresponding to  
252 the sensor positions were compared to the arrival time measured by the sensors themselves to  
253 assure the accuracy of the optical measurement in predicting the spatial and temporal  
254 variation of leading edge. The velocity was constructed by taking the difference of successive  
255 frames as explained in Rueben et al. (2010) and are used here to provide the velocity at the  
256 leading edge which was not captured by the in-situ instruments.

257         As the wave propagated around the macro-roughness, properties such as wave shape  
258 and the location of maximum free surface elevation, cross-shore velocity, and specific  
259 momentum flux, changed (Fig. 5 and Fig. 6). The maximum free surface elevation and cross-  
260 shore velocity decreased from A1 to A8 from 0.25 to 0.06 m and 2.3 to 1.6 m/s, respectively.  
261 As the wave inundated the land, the location of maximum free surface elevation occurred  
262 later in time, but the location of maximum velocity remained at the front part of the wave.  
263 The maximum specific momentum flux decreased from A1 to A8 from 0.82 to 0.05  $\text{m}^2/\text{s}^3$ ,  
264 and the locations did not coincide with either the maximum velocity or free surface elevation.  
265 Similar to the maximum free surface elevation, the location of the maximum specific  
266 momentum flux also transitioned from the front to the rear of wave as it propagated over the  
267 land.

268 Note that the specific momentum flux,  $M$ , are calculated by multiplying each time  
269 series of  $H$  by  $u^2$ , and the maximum specific momentum flux,  $(M)_m$ , taken as the maximum  
270 value over the time series. However, if  $(M)_m$  were to be calculated by multiplying the  
271 maximum value of  $H$  and,  $u$  then  $(M)_m$  would be overestimated by approximately 60% at A1  
272 and 260% at A8. The importance of correctly estimating the maximum momentum flux as it  
273 relates to hydrodynamic force on infrastructure has been discussed by FEMA (2008).

### 274 **3.1 Numerical Model**

275 There is a wide range of numerical models that could be used to simulate the Seaside  
276 experiments. Depth-integrated models, such as those based on the nonlinear shallow water  
277 (e.g. Titov and Synolakis, 1995) or Boussinesq-type (e.g. Shi *et al.*, 2012) equations are  
278 commonly used to simulate overland tsunami flow. Here, we use the model COULWAVE  
279 which solves a Boussinesq set of equations and approximately includes the effects of bottom-  
280 stress-driven turbulence with the associated vorticity (Kim *et al.*, 2009) and small-scale  
281 turbulent mixing (Kim and Lynett, 2011). The governing equations will not be repeated here,  
282 but can be found with details in the above references. A high-order finite-volume numerical  
283 solution scheme is employed to solve the conservative-form equations, and the model has  
284 been validated for wave overtopping of structures and interaction with steep slopes (Lynett *et*  
285 *al.*, 2010).

286 For the simulations presented in this paper, the wave basin is discretized with a  
287 constant and uniform grid of 5 cm and consisted of 872 by 432 points. The wave is generated  
288 along the offshore boundary by implementing a wavemaker-type condition (horizontally  
289 moving vertical wall) and is forced with the wavemaker trajectory measured during the  
290 experiment. The bathymetry and topography grid employs the lidar-surveyed data taken  
291 during the experiment, spatially averaged to fit the coarser numerical grid. It is important to  
292 note here that the individual structures and buildings in the town are approximated as steep-

293 sided topography; while in reality the sides of these buildings are vertical they are not  
294 numerically modeled as such. Many of the buildings are overtopped by the wave, and it is  
295 very difficult to numerically implement a vertical wall boundary condition and  
296 simultaneously allow dynamic overtopping. Therefore, the maximum bottom slope found in  
297 the domain can be controlled by the grid resolution, and here any side slope that exceeds 2:1  
298 (~63 degrees) is smoothed until no longer this steep. Physical implications of this steep-slope  
299 approximation include an incorrect prediction of flow properties that are dependent on locally  
300 steep slopes, such as strong vertical acceleration, uprush, and overtopping. However, results  
301 have been checked for grid-length-dependent numerical convergence.

302 The breaking model used is that described in Lynett (2006), which is very similar to  
303 the scheme given in Kennedy *et al.* (2000). Bottom stress is calculated with the common  
304 quadratic friction law, *i.e.*  $\frac{\partial u}{\partial t} + \dots + \frac{f u |u|}{H} = 0$ , where the dimensionless friction factor,  $f$ , is  
305 given as an input value, constant in both space and time throughout the simulation. The  
306 stochastic backscatter model presented in Kim and Lynett (2011) is not used in the  
307 simulations presented here. The full Boussinesq-type set of equations are solved at all points  
308 in the domain; there is no switch-off of high-order terms over initially dry grid points.

309

#### 310 **4.1 Comparison of Results and Discussions**

311 The majority of previous benchmark tests for inundation models typically compare a  
312 time series of free surface elevation or maximum run-up height, but in this study, the time  
313 series and maximum values of free surface elevation, cross-shoreline velocity, and specific  
314 momentum flux are extracted from the numerical model and directly compared with the  
315 physical model results for model verification.

316 A time series comparison of  $\langle \eta \rangle$ ,  $\langle u \rangle$  and  $\langle M \rangle$  between the physical model (dotted  
317 line) and numerical model (COULWAVE) (solid line) at B1, B4, B6, and B9 (Line B is

318 parallel to the flow direction and flanked by hotels and commercial buildings) are shown in  
319 Fig. 7, Fig. 8, and Fig. 9, respectively. There are local disagreements in free surface elevation  
320 and specific momentum flux comparison, but general tendencies and magnitudes were well  
321 matched with physical model results. Specifically, COULWAVE underestimates the free  
322 surface elevation at B1 and B4, whereas at B9 it overestimates the value. However, for  
323 specific momentum flux, COULWAVE underestimates the value at B1, and overestimates at  
324 B6 and B9.

325 To calibrate COULWAVE for these comparisons, three different friction factors,  $f =$   
326 0.001, 0.005, and 0.01 were tested. A friction factor of  $f = 0.005$  was found to produce results  
327 most similar to the physical model and was used for all subsequent analysis. The expected  
328 differences due to friction factors will be discussed in more detail in section 4.1.

329 Reflection from the model boundaries was simulated by COULWAVE. The back end  
330 of the tank in the numerical model is at a different  $x$  location than in the physical model study,  
331 and the reflection off this back wall arrives at the measurement locations earlier. Therefore,  
332 reflection effects produced by COULWAVE resulted in some erroneous data when compared  
333 to the physical model which is shown in Fig. 7, Fig. 8, and Fig. 9 (dotted lines). For example,  
334 in Fig. 7d, the magnitude of free surface elevation from COULWAVE was nearly twice as  
335 large as the physical model values due to reflection. Reflection wave effects are also  
336 observed in cross-shore velocity and specific momentum flux in Fig. 8 and Fig. 9. Fig. 10  
337 compares the maximum free surface elevation, cross-shore velocity and specific momentum  
338 flux between the numerical and physical model from B1 to B9. The  $x$ -axis represents the  
339 distance to each measurement location (B1 to B9) in the  $x$ -direction from the origin, B1. The  
340 maximum values of  $\langle \eta \rangle$ ,  $\langle u \rangle$  and  $\langle M \rangle$  were extracted at each location, and therefore, do  
341 not necessarily correspond to the same instant in time. Reflection effects present in the  
342 numerical model were excluded in the maximum value comparison. Within the first 1.5 m,

343 there are minor disagreements in the of  $\langle \eta \rangle$  and  $\langle M \rangle$ , however the numerical model values  
 344 of  $\langle M \rangle$  shows the same abrupt decrease and increase pattern between 0 and 1 m as the  
 345 physical model. Overall the physical and numerical model show good agreement. In both  
 346 models, it is observed that the maximum free surface elevation and specific momentum flux  
 347 sharply decrease from the shoreline as the measurement location moves landward, while the  
 348 cross-shore velocity slowly decreases linearly. Specifically, from B1 to B9, the maximum  
 349 free surface elevation,  $(\eta)_m$  decreases 72%, the maximum momentum flux,  $(M)_m$  decreases  
 350 96% and the maximum cross-shore velocity,  $(u)_m$  decreases 41% in physical model.

351 Fig. 11 shows the normalized root mean square errors of the numerical model  
 352 compared to the physical model at each measurement location for  $\eta$ ,  $u$ , and  $M$ , respectively.  
 353 The normalized root mean square errors are evaluated as:

$$NRMSE(\phi) = \frac{\sqrt{\frac{\sum_{i=1}^r (\hat{\phi}_i - \phi_i)^2}{r}}}{\phi_{max} - \phi_{min}}$$

354  
 355 where  $\hat{\phi}_i$  is the numerical model value,  $\phi_i$  is the physical model value,  $\phi_{max}$  and  $\phi_{min}$  are  
 356 the maximum and minimum from the physical model,  $r$  is the time step number which is less  
 357 than 1% of the maximum free surface elevation or the time step number when reflection  
 358 effects first appear, and the  $i$  is the time step for each value of  $\eta$ ,  $u$ , and  $M$ . The normalized  
 359 root mean square errors for the free surface elevation at lines A, B, and C are within 0.1,  
 360 except at C1 where it increased to 0.2, and for line D where the numerical model results  
 361 overestimated the values and are approximately 0.3 to 0.4 (Fig. 11a). Most of the normalized  
 362 root mean square errors of cross-shore velocity for lines A and D were less than 0.4, and for  
 363 lines B and C less than 0.2 (Fig. 11b). In the case of specific momentum flux, with the  
 364 exception of line D which measured around 0.8, most values are less than 0.2. Overall, with

365 the exception of line D, and line A for velocity, the normalized root mean square errors are  
366 less than 0.2.

367 The normalized root mean square errors for line D are relatively large, and in excess  
368 of four times that measured in the other three lines. This anomaly may be attributed to the  
369 difference of measurement location. Lines A, B, and C were located on the road, with no  
370 obstructions between the locations and the ocean, while line D was located mostly behind  
371 buildings. The discrepancy between lines A, B and C and line D may arise from the inherent  
372 difficulty of generating an energy dissipation process which includes turbulence in the  
373 numerical model, as the broken wave passes around the buildings.

#### 374 **4.2 Model sensitivity for friction factors.**

375 To test the numerical model sensitivity, three different friction factors,  $f = 0.001$ ,  
376  $0.005$  and  $0.01$ , were modeled, and the maximum values of free surface elevation,  $(\eta)_m$ ,  
377 velocity,  $(u)_m$ , and momentum flux,  $(M)_m$ , compared to the physical model data as a time  
378 series. Fig. 12 shows the comparison between the physical model and numerical model for  
379 these friction factors using the maximum values at B1 to B9. The  $x$ -axis represents the  
380 distance to each measurement location (B1 to B9) in the  $x$ -direction from B1. Fig. 12a shows  
381 the change in  $(\eta)_m$ , Fig. 12b shows the change in  $(u)_m$ , and Fig. 12c shows the change in  $(M)_m$ .  
382 Smaller friction factor values represent less bottom friction; therefore, increased wave  
383 magnitude and phase speed are expected as the friction factor decreases. In the numerical  
384 model, as  $f$  was decreased, the tendencies of  $(\eta)_m$ ,  $(u)_m$ , and  $(M)_m$  remained constant and  
385 overall the values increased. The values of  $(\eta)_m$  remained relatively unchanged until  $x = 4$  m  
386 (B1 to B7), after which the friction factor exhibited a greater influence. As the friction factor  
387 decreased by a factor of 10 (from 0.01 to 0.001), the maximum free surface elevation  
388 increased an average of 15%, but the cross-shore velocity and specific momentum flux  
389 increased 95 and 208%. This fact reveals that the numerical model's velocity and momentum



390 flux terms are highly sensitive to the bottom friction factor. This sensitivity is consistent with  
391 modeling of tide and storm surge predictions (*e.g.*, Westerink *et al.*, 1991) and illustrates a  
392 potential limitation to using tsunami inundation models verified with bench mark tests with  
393 only the maximum free surface elevation. Overall, a friction factor of  $f = 0.005$  (triangle) was  
394 found to provide results which best matched the physical model.

395 Fig. 13a, b, and c shows the numerical model sensitivity of  $\eta$ ,  $u$ , and  $M$ , respectively,  
396 to the three different friction factors at location B1. When the friction factor was 0.001  
397 (circle), the smallest value, the arrival time of wave was faster than the other two conditions.  
398 As the friction factor was increased, the initial magnitude of  $\eta$ ,  $u$ , and  $M$  decreased before  $t =$   
399 25.3 s, but after which all only show small changes. It appears that only the leading velocity  
400 part was dominated by the friction factors. These results could not be corroborated by the  
401 physical model data as only one friction factor was tested.

402 Fig. 14 shows the same sensitivity test as Fig. 13, but for location B4. Similar to Fig.  
403 13, the arrival time of the inundation wave was earlier and the leading velocity larger as the  
404 friction factor decreased. Unlike at location B1, the cross-shore velocity at B4 after  $t = 25.3$  s  
405 for  $f = 0.01$  was noticeably smaller than for the other two friction factors. However, there  
406 were still no discernible changes to the free surface elevation due to the various friction  
407 factors. The maximum specific momentum flux increased by more than a factor of two as the  
408 friction factor decreased from 0.01 to 0.001. This fact highlights the importance of comparing  
409 velocity terms in the validation and verification process of numerical models of tsunami  
410 inundation when evaluating velocity or force on the structures.

## 411 **5.1 Conclusion**

412 This paper presents a comparison of free surface elevation, velocity, and specific  
413 momentum flux for tsunami inundation over and around the macro-roughness of a  
414 constructed environment between a physical and numerical model (COULWAVE). The

415 physical model was a 1:50 scale idealization of Seaside, Oregon designed to observe the  
416 effects of building array and density on tsunami inundation (Fig. 2). In total the free surface  
417 elevation and velocity of the inundation flow was measured at 31 locations (Fig. 3). The  
418 design wave height was approximately 20 cm, which corresponds to the prototype scale wave  
419 height of 10 m (Fig. 4). Measured velocities at the leading edge of the wave were not  
420 recorded by the ADV, so leading velocities were determined from optical measurements  
421 (Rueben *et al.*, 2010) and interpolated velocity fitting curves applied to calculate the specific  
422 momentum flux (Fig. 5 and Fig. 6). Primary conclusions are:

423         1. As the inundating wave propagated around the macro-roughness, the wave shape  
424 and location of maximum values of free surface, velocity, and momentum flux changed. If  
425 the ensemble average specific momentum flux is calculated using the maximum values of  
426  $\langle \eta \rangle$  and  $\langle u \rangle$ , it will be overestimated by approximately 60% at A1 and 260% at A8 (Fig. 5  
427 and Fig. 6).

428         2. In general, the time series and maximum values of free surface elevation, velocity,  
429 and specific momentum flux from the numerical model show good agreement with the  
430 physical model results (Fig. 7, Fig. 8, Fig. 9, and Fig. 10) except behind the macro-roughness  
431 units (Fig. 11, line D).

432         3. Different friction factors ( $f = 0.01, 0.005$  and  $0.001$ ) were applied to test the model  
433 sensitivity. Result showed that the velocity and flux terms in the numerical model are highly  
434 sensitive to the bottom friction factor, while the free surface elevations are only slightly  
435 effected. When the friction factor decreased by a factor of 10 (from 0.01 to 0.001), the  
436 average maximum free surface elevation only increased 15%, but the average maximum  
437 cross-shore velocity and specific momentum flux increased 95 and 208%, respectively (Fig.  
438 12).

439           This research highlights the importance of comparing velocity terms in the validation  
440 and verification process of numerical models of tsunami inundation when evaluating velocity  
441 or force on structure. Future research in this area should focus on measuring pressure and  
442 force on structures to validate and improve numerical results; model the tsunami return flow,  
443 as it is known to induce scour and cause soil instability; and model complex bathymetry and  
444 topography.

445

#### 446 **Acknowledgement**

447           This material is based upon work partially supported by the National Science  
448 Foundation under Grant No. 0830378 and Oregon Sea Grant under Award No. NB223X.  
449 Any opinion, findings, and conclusions or recommendations expressed in this material are  
450 those of the authors and do not necessarily reflect the views of the National Science  
451 Foundation or Oregon Sea Grant. The authors thank two anonymous reviewers for their  
452 constructive comments.

453

454 **6.1 References**

455 Apotsos, A., Jaffe, B, and Gelfenbaum, G. (2011). "Wave Characteristic and Morphologic  
456 Effects on the Onshore Hydrodynamic Response of Tsunamis." *Coastal Engineering*  
457 58: 1034-1048.

458 Briggs, M., Synolakis, C., Harkins, G., and Green, D. (1995). "Laboratory experiments of  
459 tsunami runup on Circular Island." *Pure and Applied Geophysics* 144(3/4): 569-593.

460 Cox, D., Tomita, T., Lynett, P., and Holman, R. (2008). "Tsunami inundation with macro-  
461 roughness in the constructed environment." *Proc. 31st International Conference on*  
462 *Coastal Engineering*: 1421–1432.

463 Dalrymple, R., A., Kribel, D., L. (2005). "The Bridge – Linking Engineering and Society:  
464 Lessons in Engineering from the Tsunami in Thailand." *National Academy of*  
465 *Engineering* 35(2):4-14.

466 DOGAMI (Oregon Department of Geology and Mineral Industries), (2001). "Senate Bill  
467 379." Portland, OR. Retrieved from: Oregon Geospatial Enterprise Office (GEO).  
468 <http://cms.oregon.gov/DAS/CIO/GEO/Pages/index.aspx>

469 FEMA (Federal Emergency Management Agency) (2008). "Guidelines for Design of  
470 Structures for Vertical Evacuation from Tsunamis - FEMA P646 Report." Prepared  
471 by the Applied Technology Council for the Federal Emergency Management Agency,  
472 Redwood City, C.A..

473 Goldfinger, C., Nelson, C. H., Morey, A. E., Johnson, J. E., Patton, J. R., Karabanov, E., et al.  
474 (2012). "Turbidite Event History—Methods and Implications for Holocene  
475 Paleoseismicity of the Cascadia Subduction Zone." U.S. Geological Survey  
476 Professional Paper 1661–F, 170 p.

- 477 Goseberg, N., and Schlurmann, T. (2010). "Numerical and experimental study on tsunami  
478 run-up and inundation influenced by macro roughness elements." Proceedings of the  
479 International Conference on Coastal Engineering, 32.
- 480 Hokkaido Tsunami Survey Group (1993). "Tsunami devastates Japanese coastal region."  
481 EOS Trans. Amer. Geophys. Un. 74(37), 417 and 432.
- 482 Hughes, S. (1993). *Physical Models and Laboratory Techniques in Coastal Engineering*.  
483 Advanced Series on Ocean Engineering – Volume 7, World Scientific.
- 484 Imamura, F., Koshimura, S., Goto, K., Yanagisawa, H., and Iwabuchi, Y. (2006). "Global  
485 disaster due to the 2004 Indian Ocean tsunami." Journal of Disaster Research 1(1):  
486 131-135.
- 487 Jaffe, B., and Gelfenbuam, G. (2007). "A simple model for calculating tsunami flow speed  
488 from tsunami deposits." Sedimentary Geology 200: 347-361.
- 489 Kânoğlu, U., and Synolakis, C., E.(1998). "Long wave runup on piecewise linear  
490 topographies." Journal of Fluid Mechanics 374: 1-28.
- 491 Kennedy, A. B., Chen, Q., Kirby, J. T., and Dalrymple, R. A. (2000). "Boussinesq modeling  
492 of wave transformation, breaking and runup. I: 1D." J. Waterw., Port, Coastal, Ocean  
493 Eng., 1261, 39–47.
- 494 Kim, D.-H., Lynett, P., and Socolofsky, S. (2009). "A Depth-Integrated Model for Weakly  
495 Dispersive, Turbulent, and Rotational Fluid Flows." Ocean Modeling, v. 27 (3-4), p.  
496 198-214.
- 497 Kim, D.-H. and Lynett, P. (2011). "Turbulent Mixing and Scalar Transport in Shallow and  
498 Wavy Flows," Physics of Fluids, v. 23 (1), doi:10.1063/1.3531716.
- 499 Koshimura, S., Oie, T., Yanagisawa, H., Imamura, F. (2009)a. "Developing fragility  
500 functions for tsunami damage estimation using numerical model and post-tsunami  
501 data from banda aceh, Indonesia." Coastal Engineering Journal 51(3): 243-273.

- 502 Koshimura, S., Namegaya, Y., Yanagisawa, H. (2009)b. "Tsunami fragility: A new measure  
503 to identify tsunami damage." *Journal of Disaster Research* 4(6): 479-488.
- 504 Liu, P., Yeh, H., and Synolakis, C. (2008). *Advanced numerical models for simulation  
505 tsunami and runup*. Singapore, World Scientific Publishing.
- 506 Lynett, P. (2006). "Nearshore Modeling Using High-Order Boussinesq Equations," *Journal of  
507 Waterway, Port, Coastal, and Ocean Engineering (ASCE)*, v. 132(5), p. 348-357
- 508 Lynett, P. (2007). "Effect of a shallow water obstruction on long wave runup and overland  
509 flow velocity." *Journal of Waterway, Port, Coastal, and Ocean Engineering* 133(6):  
510 455-462.
- 511 Lynett, P., Wu, T., and Liu, P. (2002). "Modeling wave runup with depth-integrated  
512 equations." *Coastal Engineering* 46: 89-107.
- 513 Lynett, P., Melby, J., and Kim, D.-H. "An Application of Boussinesq Modeling to Hurricane  
514 Wave Overtopping and Inundation," *Ocean Engineering*. v. 37, p. 135-153. 2010.
- 515 Matstomi, H., and Okamoto, K. (2010). "Inundation flow velocity of tsunami on land." *Island  
516 Arc* 19: 443-457.
- 517 Moore, A., McAdoo, B., and Ruffman, A. (2007). "Landward fining from multiple sources in  
518 a sand sheet deposited by the 1929 Grand Banks tsunami, Newfoundland."  
519 *Sedimentary Geology* 200: 336-346.
- 520 Mori, N., Takahashi, T., Yasuda, T., and Yanagisawa, H. (2011). "Survey of 2011 Tohoku  
521 earthquake tsunami inundation and run-up." *Geophysical Research Letters*, 38.
- 522 Nandasena, N., A., K., Sasaki, Y., Tanaka, N. (2012). "Modeling field observations of the  
523 2011 Great East Japan tsunami: Efficacy of artificial and natural structures on  
524 tsunami mitigation." *Coastal Engineering* 67: 1-13.

- 525 National Oceanic and Atmospheric Administration (NOAA), (2012). "National Data Buoy  
526 Center." Stennis Space Center, Mississippi. Retrieved from: National Data Buoy  
527 Center. <http://www.ndbc.noaa.gov/>
- 528 Rueben, M., Holman, R., Cox, D., Shin, S., Killian, J., and Stanley, J. (2010). "Optical  
529 measurements of tsunami inundation through an urban waterfront modeled in a large-  
530 scale laboratory basin." *Coastal Engineering* 58(3): 229-238.
- 531 Shi, Fengyan, Kirby, T., James, Harris, C., Jeffrey, Geiman, D., Joseph, Grilli, T., Stephan  
532 (2012). "A high-order adaptive time-stepping TVD solver for Boussinesq modeling  
533 of breaking waves and coastal inundation." *Ocean Modelling* 43-44: 36-51.
- 534 Synolakis, C., Bernard, E., Titov, V., Kânoğlu, U., and Gonzalez, F. (2007). "Standards,  
535 criteria, and procedures for NOAA evaluation of tsunami numerical models."  
536 Commerce, NOAA Tech. OAR PMEL-135.
- 537 Synolakis, C. a. R., F. (2003). "Waves and Run-Up Generated By a Three-Dimensional  
538 Sliding Mass." *Advances in Natural and Technological Hazards Research* 19(1):  
539 113-119.
- 540 Synolakis, C. E. (1987). "The runup of solitary waves." *Journal of Fluid Mechanics* 185: 523-  
541 545.
- 542 Titov, V.V., Synolakis, C.E. (1995). Modeling of breaking and non-breaking long wave  
543 evolution and runup using VTCS-2. *J. Waterw. Port Coast. Ocean Eng.* 121, 308-  
544 316.
- 545 Tomita, T., and Honda, K. (2007). "Tsunami estimation including effect of coastal structures  
546 and buildings by 3D model." *Coastal Structures 2007*: 681-692.
- 547 Tomita, T., Honda, K., and Kakinuma, T. (2006). "Application of storm surge and tsunami  
548 simulator in ocean and coastal areas (STOC) to tsunami analysis." *Technical*  
549 *Memorandum of Public Works Research Institute* 4022.

- 550 Tsunami Pilot Study Working Group (2006). "Seaside, Oregon Tsunami Pilot Study—  
551 Modernization of FEMA Flood Hazard Maps." NOAA OAR Special Report,  
552 NOAA/OAR/PMEL, Tsunami Pilot Study Working Group
- 553 Westerink, J.J., Luetlich, R.A., Baptista, A.M., Scheffner, N.W., and Farrar, P. (1992) "Tide  
554 and Storm Surge Predictions Using Finite Element Model," Journal Hydraulic  
555 Engineering, 118, 10, 1373-1390.
- 556 Yeh, H., Sato, S., Tajima, Y. (2012). "The 11 March 2011 East Japan Earthquake and  
557 Tsunami: Tsunami Effects on Coastal Infrastructure and Buildings". Pure and  
558 Applied Geophysics.
- 559 Yeh, H. (2006). "Maximum fluid forces in the tsunami runup zone." Journal of Waterway, Port,  
560 Coastal, and Ocean Engineering 132(6): 496-500.
- 561 Yeh, H., Liu, P., and Synolakis, C. (1996). *Long-wave runup models*. Singapore, World  
562 Scientific.
- 563
- 564
- 565
- 566
- 567
- 568
- 569
- 570
- 571
- 572
- 573
- 574



575 **Nomenclature**

| 576 | Symbol            | Description  | Units       |
|-----|-------------------|--|-------------|
|     | $f$               | Friction factor  | -           |
|     | $H$               | Total water depth  | L           |
|     | $h$               | Vertical datum   | L           |
|     | $M$               | Momentum flux per unit mass per unit width                       | $L^3T^{-2}$ |
|     | $N_T$             | Number of experiment trials for each measuring location          | L           |
|     | $N_V$             | Available number of measurement data for each measuring location | L           |
|     | $N_\eta$          | Recorded number of free surface elevation at each time step.     | L           |
|     | $N_u$             | Recorded number of cross-shore velocity at each time step.       | L           |
|     | $NRMSE$           | Normalized root mean square error value                          | -           |
|     | $S$               | Wave maker displacement  | L           |
|     | $s$               | Second   | T           |
|     | $u$               | Cross-shore (x-axis) velocity                                    | $LT^{-1}$   |
|     | $u_L$             | Leading wave velocity  | $LT^{-1}$   |
|     | $v$               | Along-shore (y-axis) velocity                                    | $LT^{-1}$   |
|     | $w$               | Vertical (z-axis) velocity                                       | $LT^{-1}$   |
|     | $x$               | x-coordinate in the experiment                                   | L           |
|     | $y$               | y-coordinate in the experiment                                   | L           |
|     | $\eta$            | Free surface elevation   | L           |
|     | $\eta_w$          | Free surface elevation at wavemaker                              | L           |
|     | $\sigma_i$        | Standard deviation at the specific time, $i$                     | L           |
|     | $X_i$             | Specific measured values (Surface elevation) at the time, $i$    | L           |
|     | $\langle \rangle$ | Ensemble averaged value  | -           |
|     | $( )_m$           | Maximum value of ( )   | -           |

577

578 **List of Figures**

579 Fig. 1. Seaside, Oregon. Main map, shows the 1:50 physical model region (dash-dot), macro-  
 580 roughness region (dash), and tsunami inundation line (solid). Inset map shows  
 581 regional location of Seaside, location of offshore DART buoys, and proximity to the  
 582 Cascadia Subduction Zone (solid-triangle).

583 Fig. 2. Plan and elevation view of the physical model in the Tsunami Wave basin. Satellite  
 584 imagery (source from Google), and a laboratory photo provide the scale of the  
 585 Seaside, OR, model.

586 Fig. 3. Detailed plan view of macro-roughness elements of the physical model, annotated  
 587 with measurement locations.

588 Fig. 4. Time series plots for Trial #51. (a) Wave-maker paddle displacement,  $S$ , (solid line)  
 589 and free surface elevation on paddle multiplied by a factor of 5,  $5\eta$  (dashed line). (b) ,  
 590  $\eta$  at WG1 (solid line) and at WG3 (dashed line). (c)  $\eta$  at A1 (solid line) and at C1  
 591 (dashed line). (d)  $u$  at A1 (solid line, down) and at C1 (dashed line, upper).

592 Fig. 5. Measured and calculated inundation flow data at A1. (a): Ensemble averaged free  
 593 surface elevation,  $\langle\eta\rangle$  (dot), ensemble averaged velocity,  $\langle u\rangle$  (circle), ensemble  
 594 averaged specific momentum flux,  $\langle M\rangle$  (thick line), leading wave velocity from  
 595 optical measurement,  $u_L$  (filled circle), fitted curve for  $\langle u\rangle$  (slender line). (b):  
 596 Number of recorded free surface elevation at each time step,  $N_\eta$  (dot) and number of  
 597 recorded cross-shore velocity at each time step,  $N_u$  (circle). Number of data recorded  
 598 at each time step from USWG (dot) and ADV (circle).

599 Fig. 6. Measured and calculated inundation flow data at A8. (a): Ensemble averaged free  
 600 surface elevation,  $\langle\eta\rangle$  (dot), ensemble averaged velocity,  $\langle u\rangle$  (circle), ensemble  
 601 averaged specific momentum flux,  $\langle M\rangle$  (thick line), leading wave velocity from  
 602 optical measurement,  $u_L$  (filled circle), and interpolated velocity (slender line). (b):

603 Number of recorded free surface elevation at each time step,  $N_\eta$  (dot) and number of  
 604 recorded cross-shore velocity at each time step,  $N_u$  (circle). Number of data recorded  
 605 at each time step from USWG (dot) and ADV (circle).

606 Fig. 7. Comparison of  $\langle \eta \rangle$  between physical model (dot) and numerical model (solid line) at  
 607 B1, B4, B6 and B9. Where wave reflection is present in the numerical model, the  
 608 solid line switches to a dashed line.

609 Fig. 8. Comparison of  $\langle u \rangle$  between physical model (circle) and numerical model (solid line)  
 610 at B1, B4, B6 and B9 with the leading velocity from optical measurement (filled  
 611 circle). Where wave reflection is present in the numerical model, the solid line  
 612 switches to a dashed line.

613 Fig. 9. Comparison of  $\langle M \rangle$  between physical model (thick solid line) and numerical model  
 614 (solid) at B1, B4, B6 and B9. Where wave reflection is present in the numerical  
 615 model, the solid line switches to a dashed line.

616 Fig. 10. Comparison of the maximum values between physical model (filled triangle) and  
 617 numerical model (unfilled triangle) for line B. (a): Maximum free surface elevation,  
 618  $(\eta)_m$ . (b): Maximum cross-shore velocity,  $(u)_m$ . (c): Maximum specific momentum  
 619 flux,  $(M)_m$ .

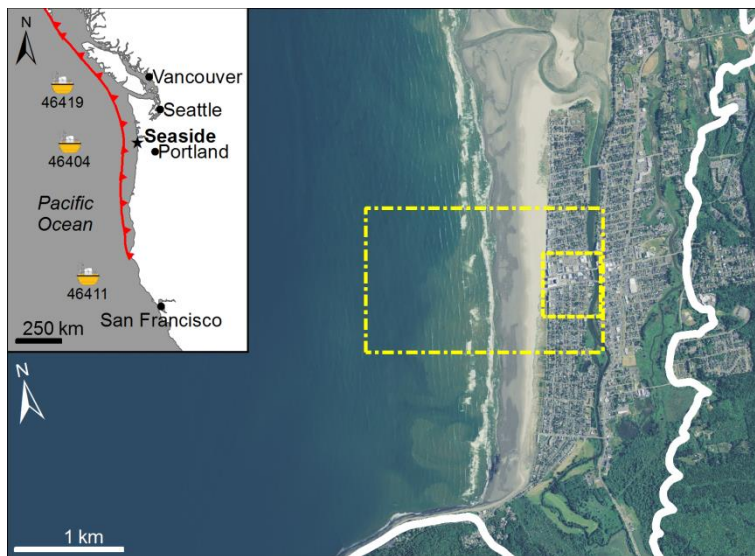
620 Fig. 11. Normalized root mean square errors (NRMSE) of numerical results at lines A, B, C,  
 621 and D (circle, triangle, square, and diamond). (a): Free surface elevation,  $\eta$ . (b):  
 622 Cross-shore velocity,  $u$ . (c): Specific Momentum flux,  $M$ .

623 Fig. 12. Numerical model sensitivity test of three friction factors,  $f = 0.001, 0.005, \text{ and } 0.01$   
 624 (circle, triangle, and square), compared to the physical model (solid line) showing  
 625 maximum values for line B. (a):  $(\eta)_m$ . (b):  $(u)_m$ . (c):  $(M)_m$ .

626 Fig. 13. Numerical model time series sensitivity test of three friction factors,  $f = 0.001, 0.005,$   
 627 and  $0.01$  (circle, triangle, and square) for location B1. (a):  $\eta$ . (b):  $u$ . (c):  $M$ .

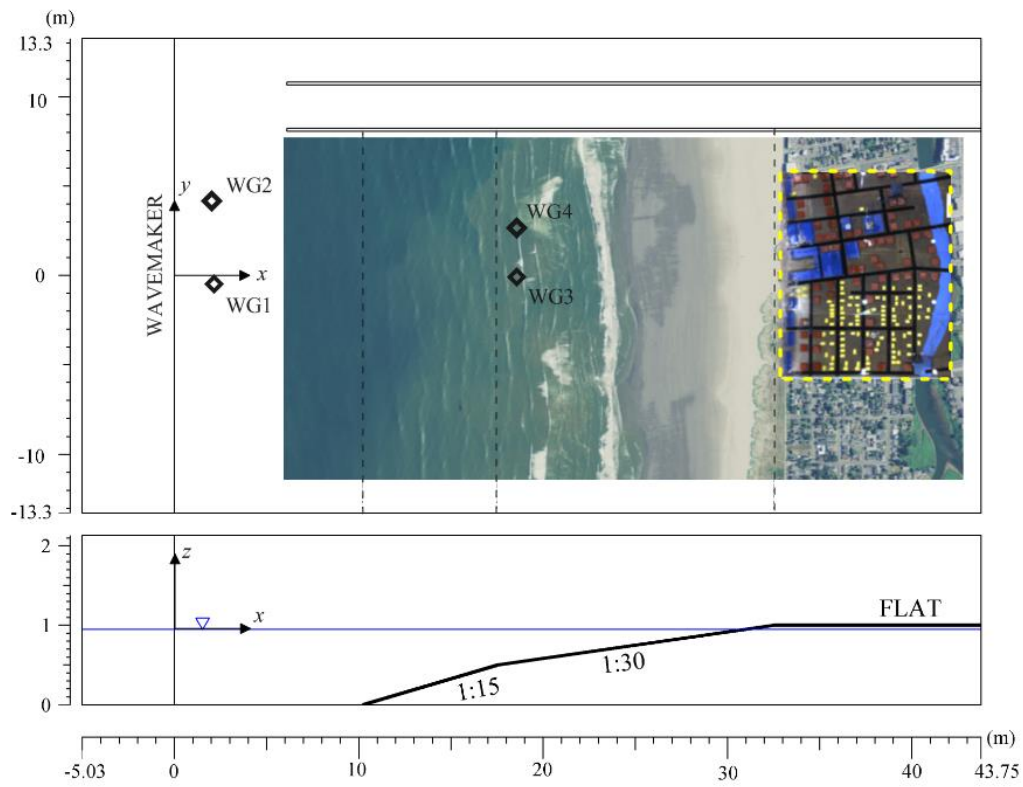
628 Fig. 14. Numerical model time series sensitivity test of three friction factors,  $f = 0.001, 0.005,$   
629 and  $0.01$  (circle, triangle, and square) for location B4. (a):  $\eta$ . (b):  $u$ . (c):  $M$ .

630



631

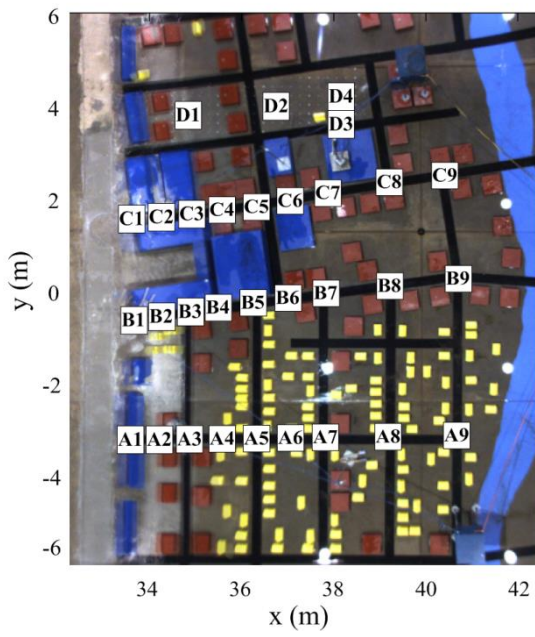
632 Fig. 1. Seaside, Oregon, Main map (Source from Google) shows the 1:50 physical model  
633 region (dash-dot), macro-roughness region (dash), and tsunami inundation line (solid). Inset  
634 map shows regional location of Seaside, location of offshore DART buoys, and proximity to  
635 the Cascadia Subduction Zone (solid-triangle).

636  
637

638

639 Fig. 2. Plan and elevation view of the physical model in the Tsunami Wave basin. Satellite  
 640 imagery (Source from Google) and a laboratory photo provide the scale of the Seaside, OR,  
 641 model.

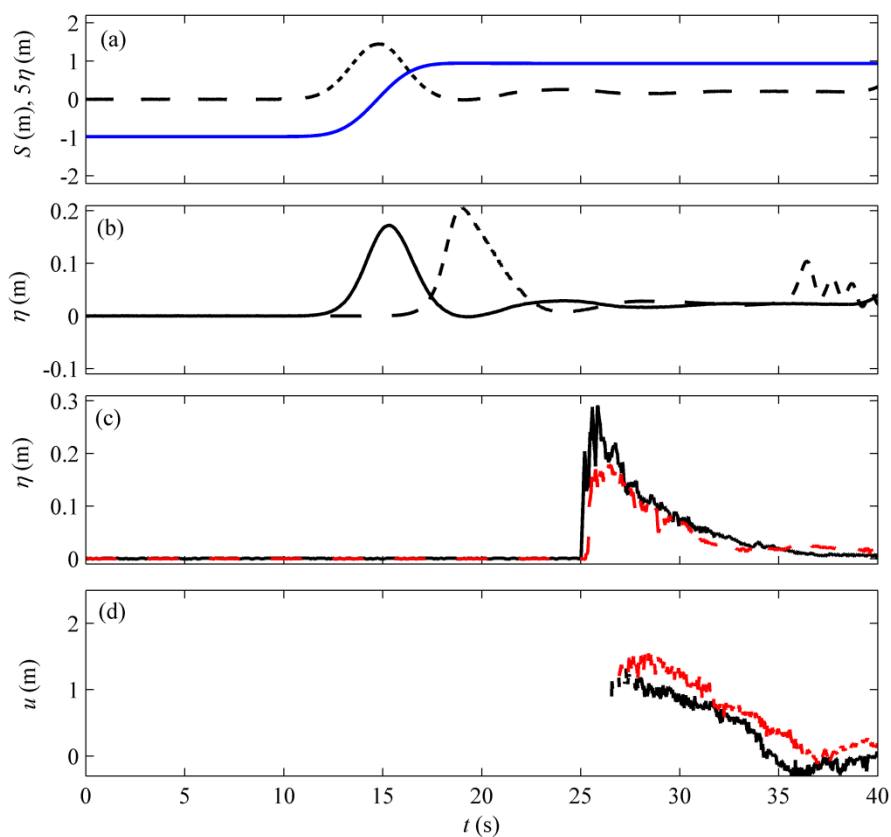
642



643

644 Fig. 3. Detailed plan view of macro-roughness elements of the physical model, annotated  
645 with measurement locations.

646

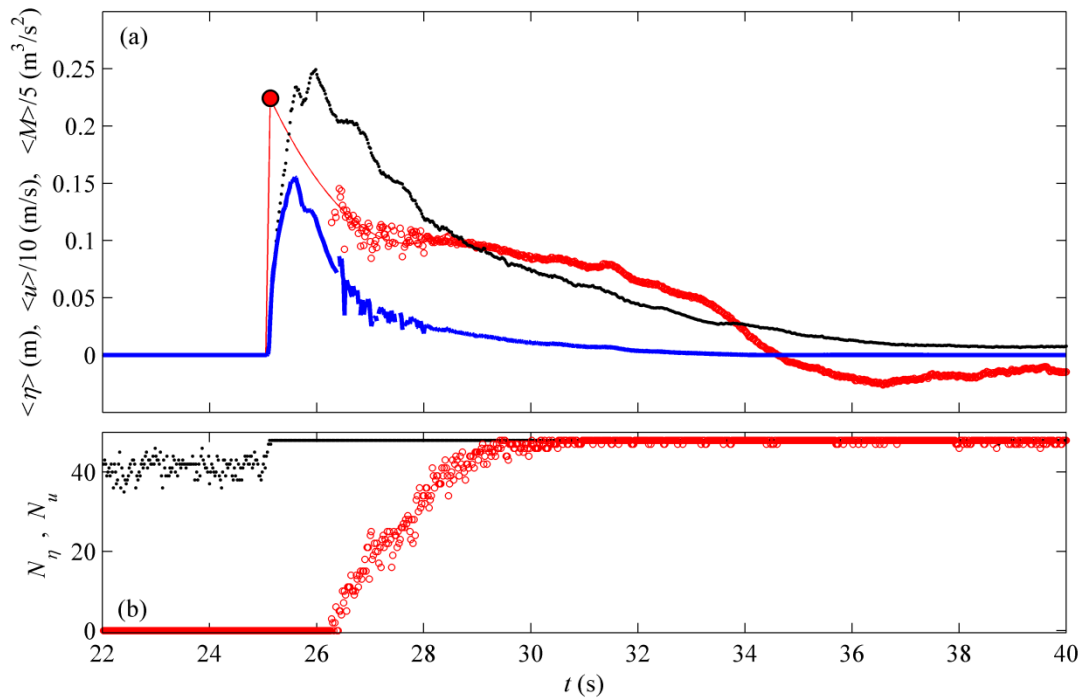


647

648 Fig. 4. Time series plots for Trial #51. (a) Wave-maker paddle displacement,  $S$ , (solid line)  
 649 and free surface elevation on paddle multiplied by a factor of 5,  $5\eta$  (dashed line). (b)  $\eta$ , at  
 650 WG1 (solid line) and at WG3 (dashed line). (c)  $\eta$  at A1 (solid line) and at C1 (dashed line).  
 651 (d)  $u$  at A1 (solid line, down) and at C1 (dashed line, upper).



652



653

654

655

656

657

658

659

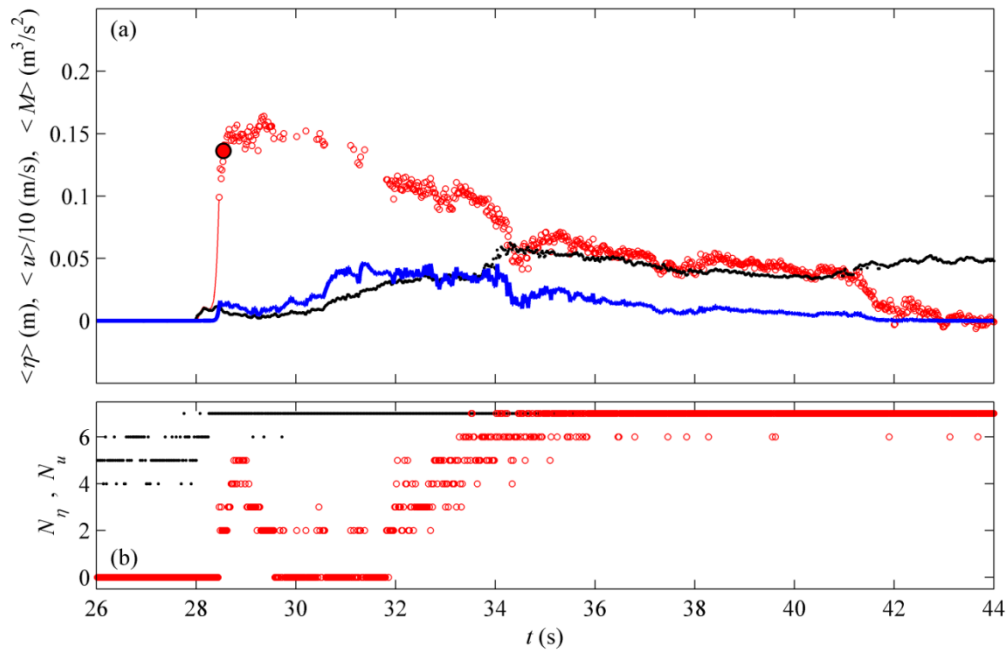
660

661

661

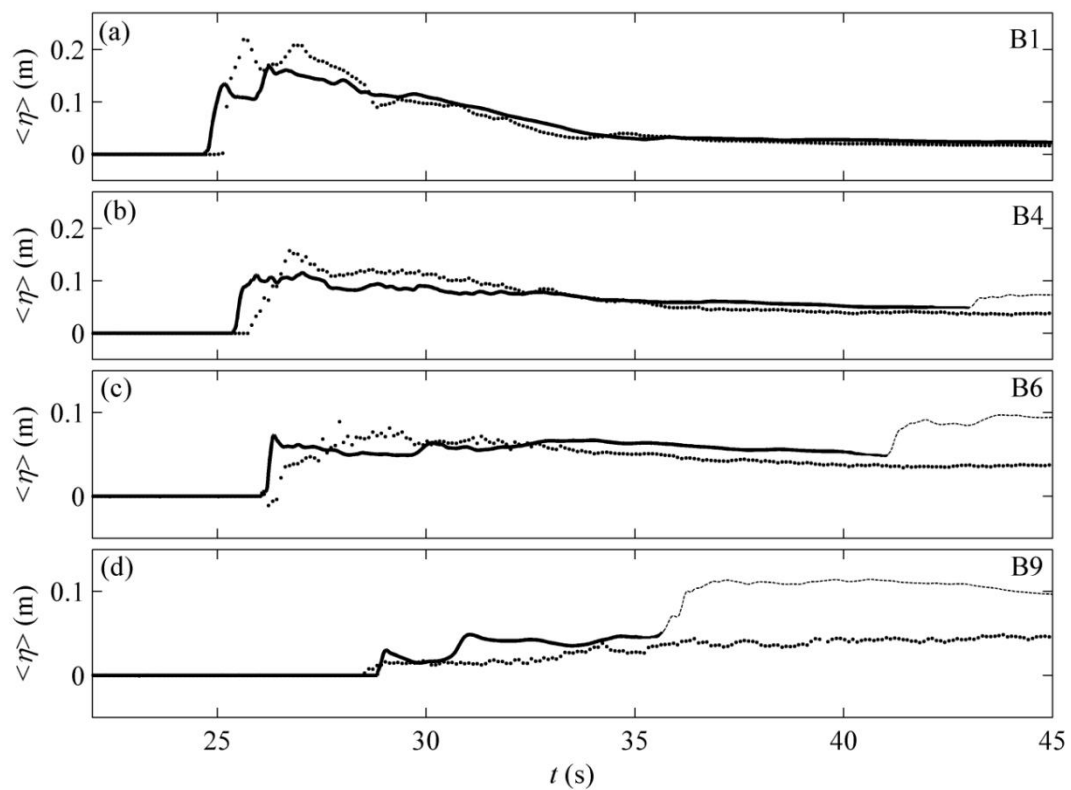
Fig. 5. Measured and calculated inundation flow data at A1. (a): Ensemble averaged free surface elevation,  $\langle \eta \rangle$  (dot), ensemble averaged velocity,  $\langle u \rangle$  (circle), ensemble averaged specific momentum flux,  $\langle M \rangle$  (thick line), leading wave velocity from optical measurement,  $u_L$  (filled circle), fitted curve for  $\langle u \rangle$  (slender line). (b): Number of recorded free surface elevation at each time step,  $N_\eta$  (dot) and number of recorded cross-shore velocity at each time step,  $N_u$  (circle). Number of data recorded at each time step from USWG (dot) and ADV (circle).

662



663

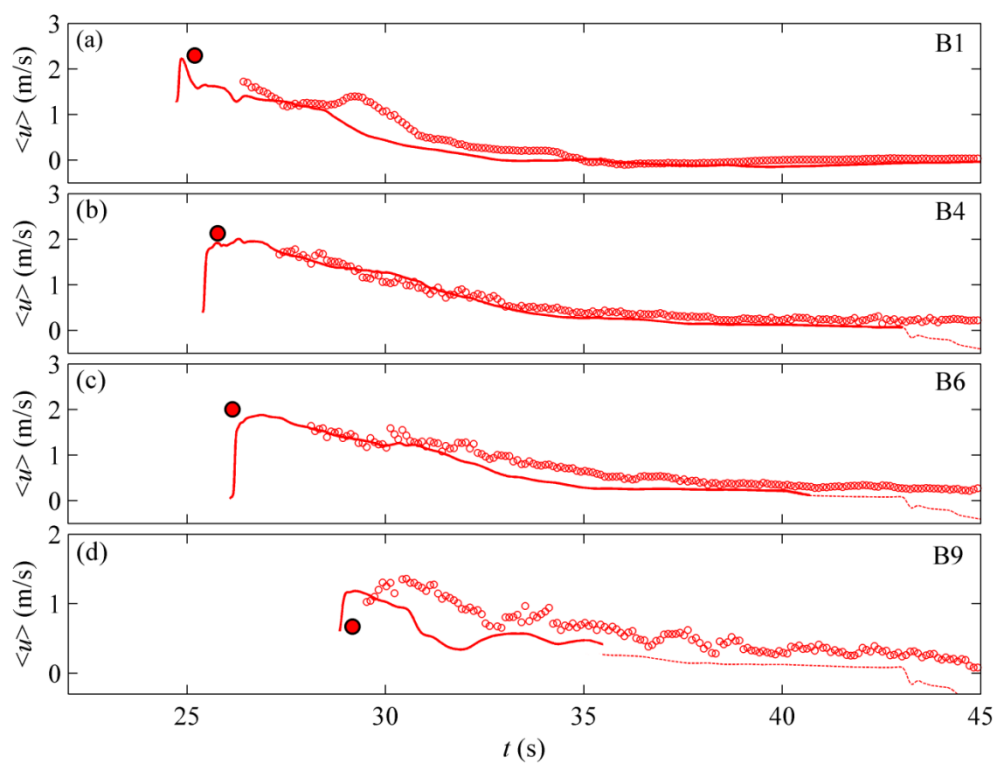
664 Fig. 6. Measured and calculated inundation flow data at A8. (a): Ensemble averaged free  
 665 surface elevation,  $\langle \eta \rangle$  (dot), ensemble averaged velocity,  $\langle u \rangle$  (circle), ensemble averaged  
 666 specific momentum flux,  $\langle M \rangle$  (thick line), leading wave velocity from optical measurement,  
 667  $u_L$  (filled circle), and interpolated velocity (slender line). (b): Number of recorded free surface  
 668 elevation at each time step,  $N_\eta$  (dot) and number of recorded cross-shore velocity at each time  
 669 step,  $N_u$  (circle). Number of data recorded at each time step from USWG (dot) and ADV  
 670 (circle).  
 671



672

673 Fig. 7. Comparison of  $\langle \eta \rangle$  between physical model (dot) and numerical model (solid line) at  
674 B1, B4, B6 and B9. Where wave reflection is present in the numerical model, the solid line  
675 switches to a dashed line.

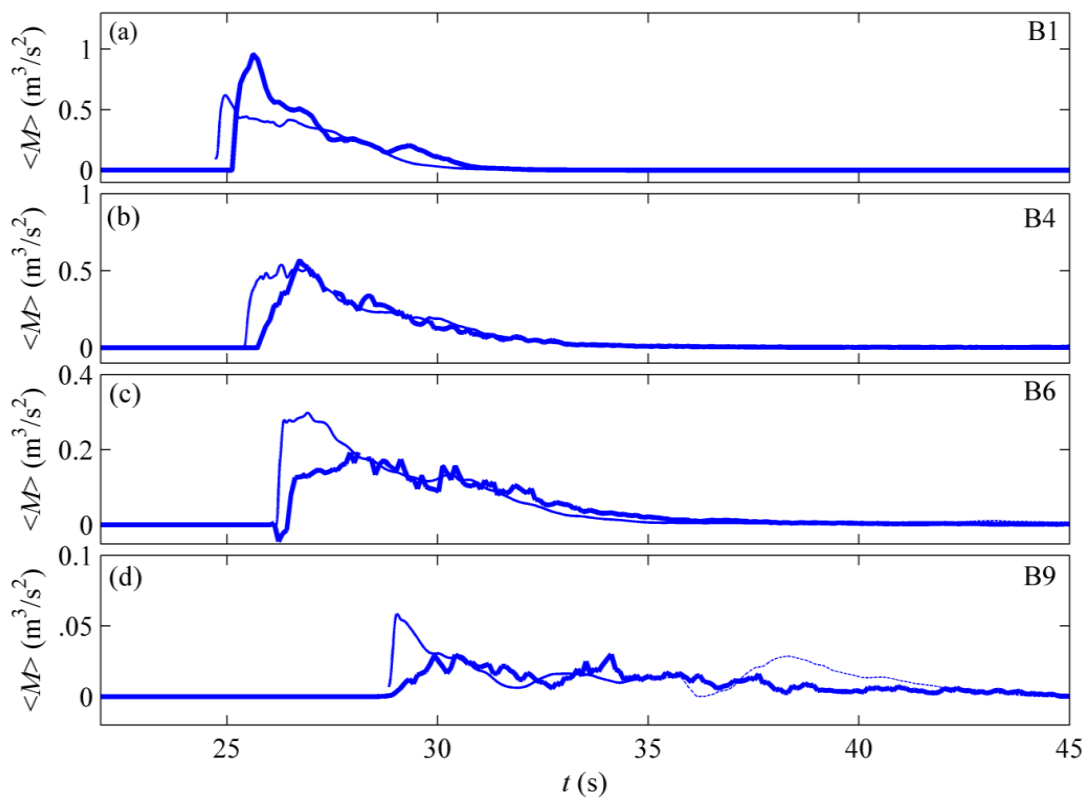
676



677

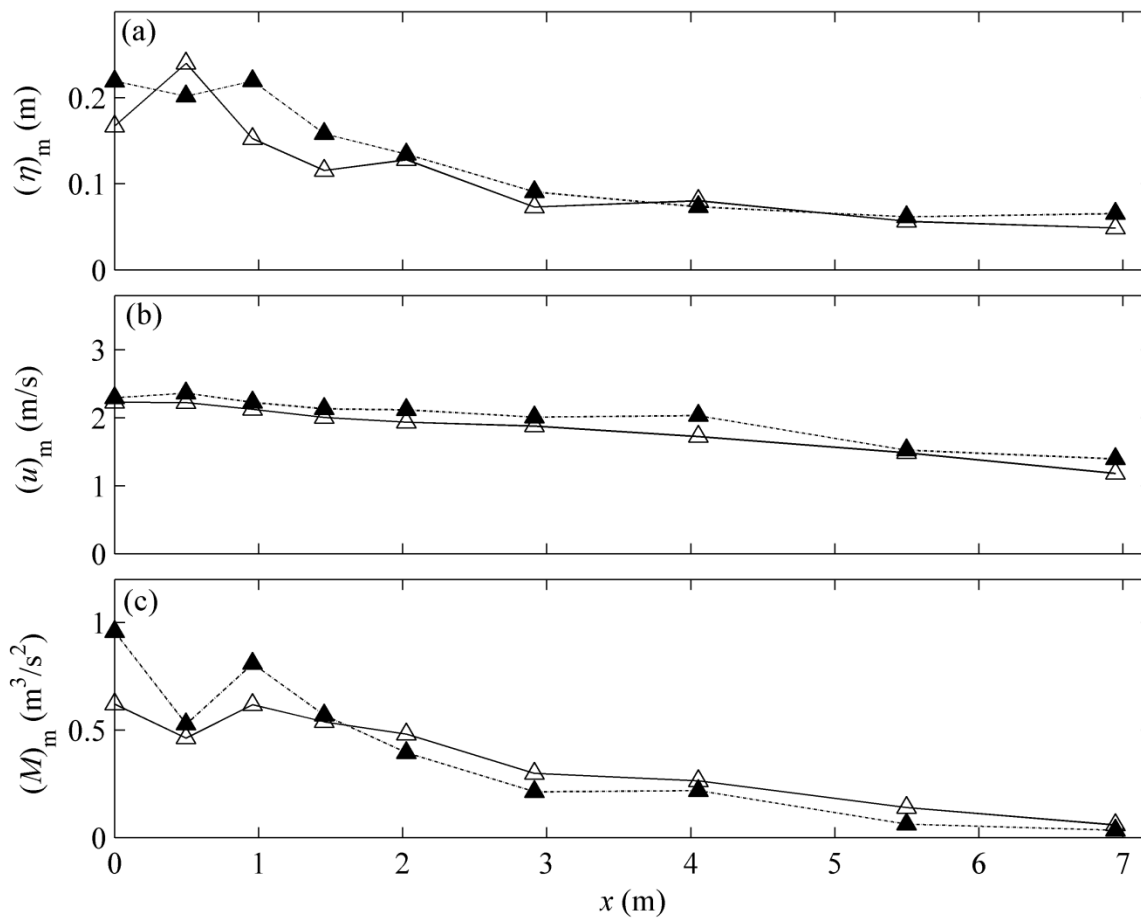
678 Fig. 8. Comparison of  $\langle u \rangle$  between physical model (circle) and numerical model (solid line)  
 679 at B1, B4, B6 and B9 with the leading velocity from optical measurement (filled circle).  
 680 Where wave reflection is present in the numerical model, the solid line switches to a dashed  
 681 line.

682



683

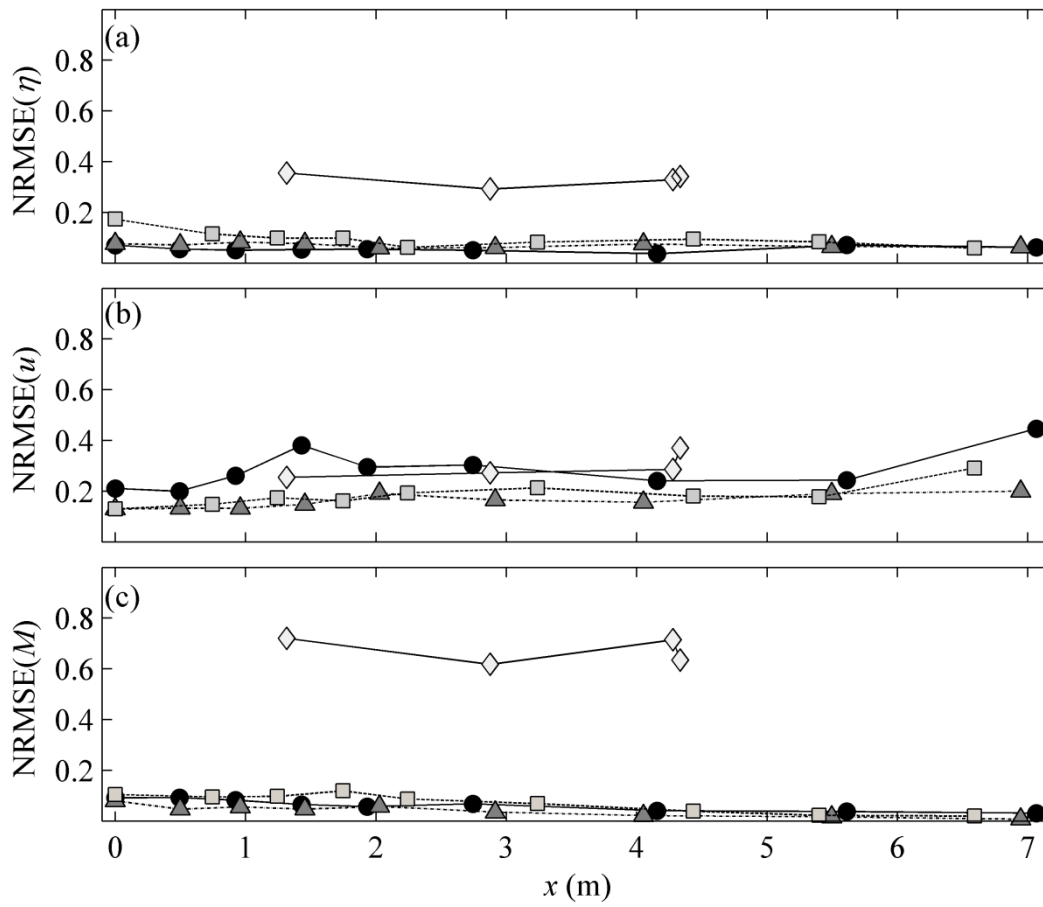
684 Fig. 9. Comparison of  $\langle M \rangle$  between physical model (thick solid line) and numerical model  
 685 (solid) at B1, B4, B6 and B9. Where wave reflection is present in the numerical model, the  
 686 solid line switches to a dashed line.



687

688 Fig. 10. Comparison of the maximum values between physical model (filled triangle) and  
 689 numerical model (unfilled triangle) for line B. (a): Maximum free surface elevation,  $(\eta)_m$ . (b):  
 690 Maximum cross-shore velocity,  $(u)_m$ . (c): Maximum specific momentum flux,  $(M)_m$ .

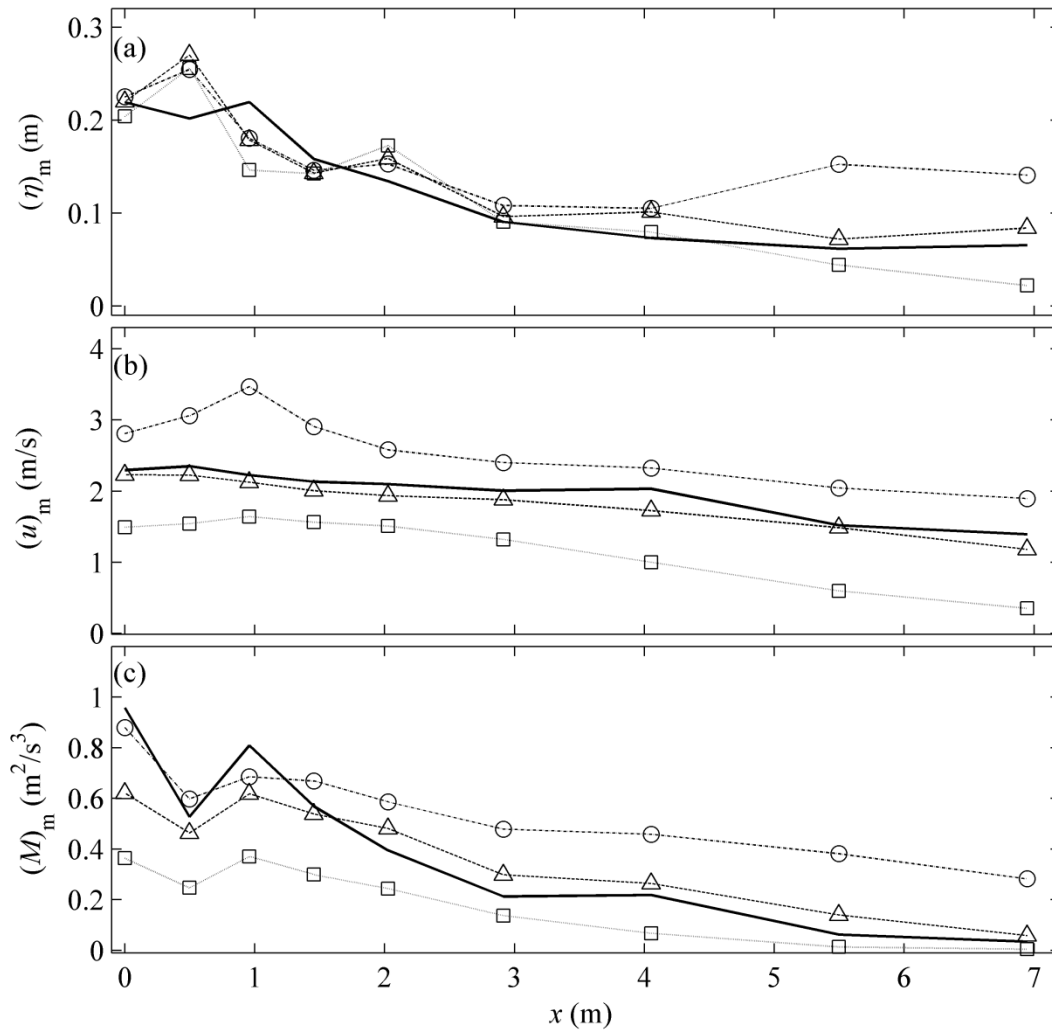
691



692

693 Fig. 11. Normalized root mean square errors (NRMSE) of numerical results at lines A, B, C,  
 694 and D (circle, triangle, square, and diamond). (a): Free surface elevation,  $\eta$ . (b): Cross-shore  
 695 velocity,  $u$  (c): Specific momentum flux,  $M$ .

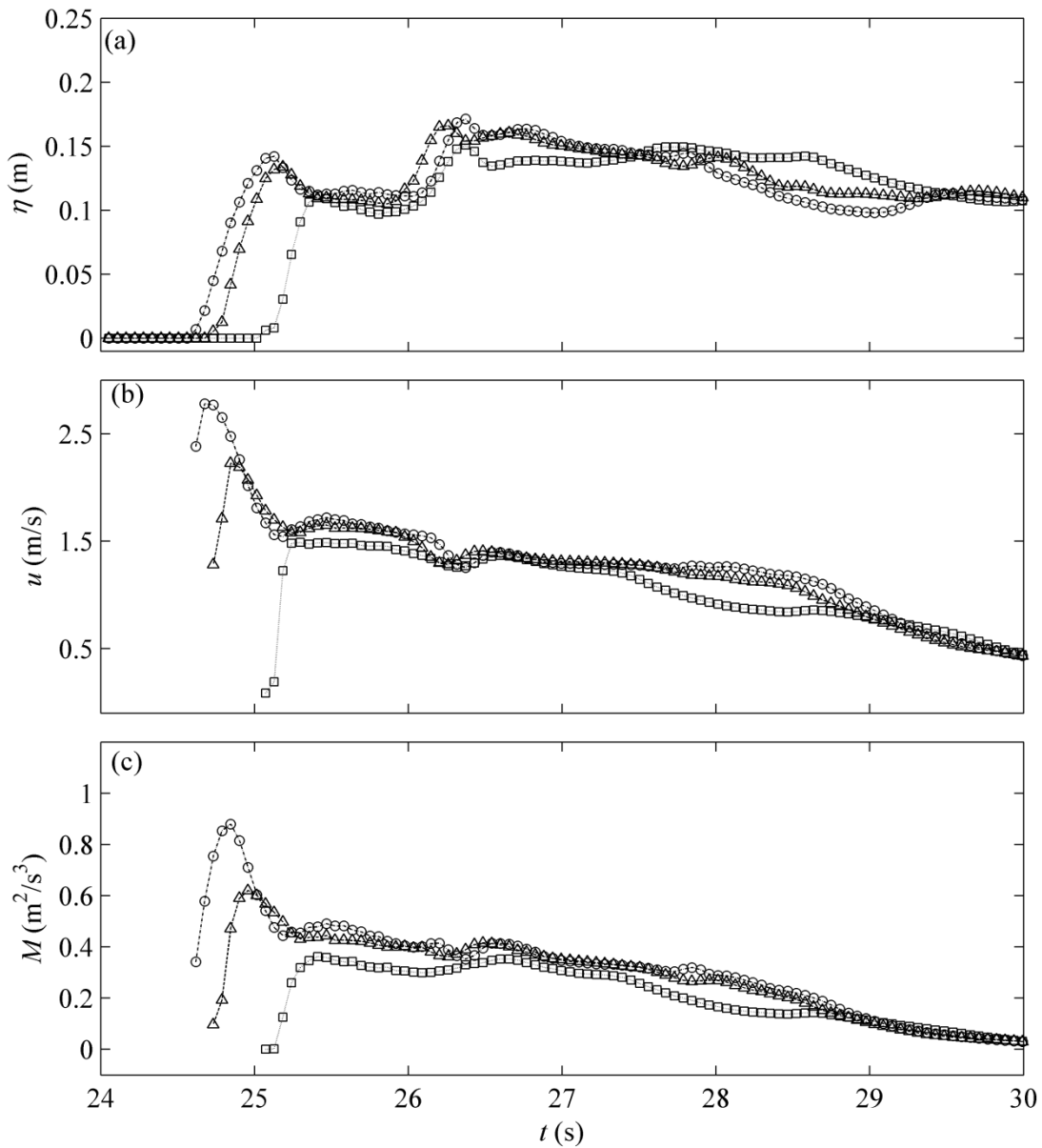
696



697

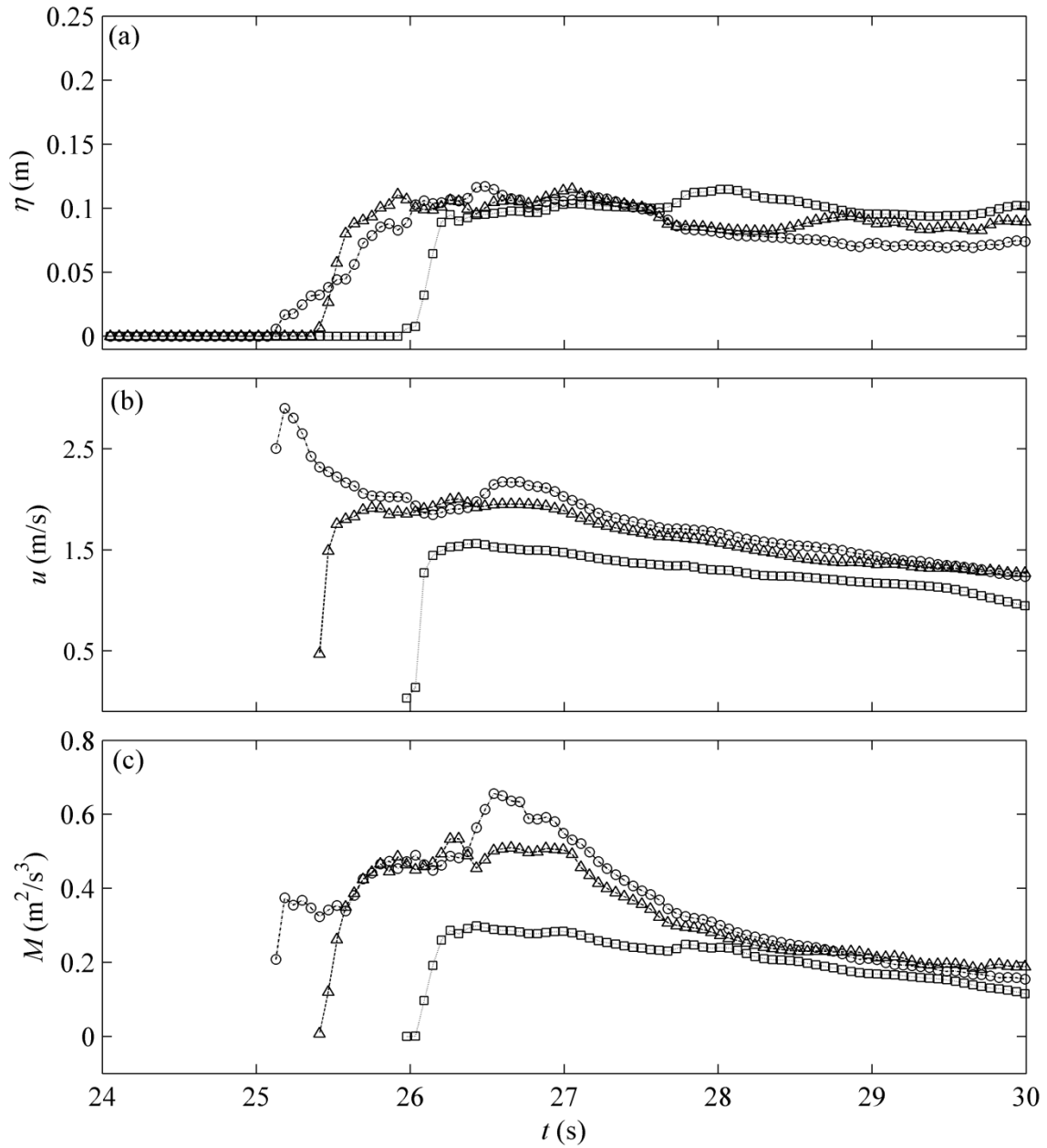
698 Fig. 12. Numerical model sensitivity test of three friction factors,  $f = 0.001, 0.005,$  and  $0.01$   
 699 (circle, triangle, and square), compared to the physical model (solid line) showing maximum  
 700 values for line B. (a):  $(\eta)_m$ . (b):  $(u)_m$ . (c):  $(M)_m$



701  $(M)_m$ 

702

703 Fig. 13. Numerical model time series sensitivity test of three friction factors,  $f = 0.001$ ,  $0.005$ ,704 and  $0.01$  (circle, triangle, and square) for location B1. . (a):  $(\eta)_m$ . (b):  $(u)_m$ . (c):  $(M)_m$ .



705

706 Fig. 14. Numerical model time series sensitivity test of three friction factors,  $f = 0.001, 0.005,$   
 707 and  $0.01$  (circle, triangle, and square) for location B4. (a):  $(\eta)_m$ . (b):  $(u)_m$ . (c):  $(M)_m$ .

708

709

710 **List of Tables**

711 Table 1. Measurement locations and numbers of total and available trials,  $NT$  and  $NV$ , respectively.

712 Table 2. Standard deviation of the signal to the full scale value for the wavemaker (S), free surface

713 prior to breaking (WG 1, 3) and after breaking (A1, D1, D4).

714

715 Table 1. Measurement locations and numbers of total and available trials,  $N_T$  and  $N_V$ , respectively.

| Num.         | Line A  |         | Line B  |         | Line C  |         | A, B, & C |       | Num. | Line D  |         |       |                  |
|--------------|---------|---------|---------|---------|---------|---------|-----------|-------|------|---------|---------|-------|------------------|
|              | $x$ (m) | $y$ (m) | $x$ (m) | $y$ (m) | $x$ (m) | $y$ (m) | $N_T$     | $N_V$ |      | $x$ (m) | $y$ (m) | $N_T$ | $N_V$            |
| 1            | 33.61   | -3.19   | 33.72   | -0.59   | 33.81   | 1.51    | 53        | 48    | 1    | 35.12   | 3.71    | 53    | 48 <sup>i</sup>  |
| 2            | 34.10   | -3.19   | 34.22   | -0.53   | 34.55   | 1.60    | 11        | 10    | 2    | 36.68   | 3.89    | 33    | 26 <sup>ii</sup> |
| 3            | 34.53   | -3.18   | 34.68   | -0.47   | 35.05   | 1.69    | 12        | 12    |      |         |         |       |                  |
| 4            | 35.04   | -3.18   | 35.18   | -0.41   | 35.56   | 1.77    | 12        | 4     |      |         |         |       |                  |
| 5            | 35.54   | -3.19   | 35.75   | -0.32   | 36.05   | 1.85    | 18        | 5     | 3    | 38.09   | 4.07    | 18    | 5 <sup>iii</sup> |
| 6            | 36.35   | -3.20   | 36.64   | -0.23   | 37.05   | 1.99    | 7         | 6     | 4    | 38.14   | 3.59    | 28    | 20 <sup>iv</sup> |
| 7            | 37.76   | -3.20   | 37.77   | -0.07   | 38.24   | 2.19    | 6         | 3     |      |         |         |       |                  |
| 8            | 39.22   | -3.20   | 39.22   | 0.14    | 39.21   | 2.34    | 8         | 7     |      |         |         |       |                  |
| 9            | 40.67   | -3.23   | 40.67   | 0.27    | 40.40   | 2.58    | 9         | 4     |      |         |         |       |                  |
| <b>Total</b> |         |         |         |         |         |         | 136       | 99    |      |         |         | 136   | 99               |

716 \*i) Corresponds to line A to C Num. 1; ii) Corresponds to lines A to C Num. 2, 3 and 4; iii) Corresponds to lines

717 A to C Num. 5; iv) Corresponds to lines A to C Num. 6, 7, 8 and 9

718 \*\* Ensemble averaged data at all 31 measurement locations are available by contacting the first author.

719

720 Table 2. Standard deviation of the signal to the full scale value for the wavemaker ( $S$ ),  
 721 free surface prior to breaking (WG 1, 3) and after breaking (A1, D1, D4).  
 722

| <b>Variables</b> | $\sigma_i$<br>[m] | $(X_i)_m$<br>[m] | $\sigma_i / (X_i)_m$<br>[-] |
|------------------|-------------------|------------------|-----------------------------|
| S                | 0.0002            | 1.889            | 0.14                        |
| WG1              | 0.0017            | 0.170            | 0.99                        |
| WG3              | 0.0023            | 0.201            | 1.13                        |
| A1               | 0.0149            | 0.271            | 5.50                        |
| D1               | 0.0027            | 0.052            | 5.11                        |
| D4               | 0.0038            | 0.046            | 8.25                        |

723